Journal of the Brazilian Society of Mechanical Sciences and Engineering (2021) 43:160
https://doi.org/10.1007/s40430-021-02848-2

TECHNICAL PAPER

Aerodynamic improved design and optimization for the rear stage of a High-load axial compressor

Hang Xiang[1] · Jiang Chen[1] · Jinxin Cheng[2] · Han Niu[1] · Yi Liu[1] · Xiancheng Song[3]

Received: 28 May 2020 / Accepted: 1 January 2021 / Published online: 24 February 2021

Abstract
This paper proposes and discusses the aerodynamic retrofit design schemes for a multistage high pressure axial compressor. A high hub/tip ratio mixed-flow compressor is designed and analyzed to replace the rear stage of the axial compressor. In order to minimize the axial dimension and maximize the load capacity, three unconventional types of combined compressors equipped with the high hub/tip ratio mixed-flow compressor are explored. Further, the effects of blade number, splitter blades and dimensionless geometric parameters on the mixed-flow compressor performance are investigated by an improved loss model. A full-surface parameterization control method is introduced and adopted for blade optimizations of the mixed-flow impeller and the tandem stator. The results indicate that after aerodynamic improved design and optimization, the total pressure ratio is relatively improved by 3.71% and the adiabatic efficiency is improved by 0.95 percent point for the mixed-flow compressor at the near design point. Based on this, the retrofit schemes for the axial compressor are beneficial to improve the load capacity and reduce the axial dimension with a slight impact on efficiency and surge margin. These show the potential application prospects of high hub/tip ratio mixed-flow compressors.

Keywords Axial compressor · Mixed-flow compressor · Hub/tip ratio · Retrofit design · Full-surface parameterization · Optimization

Abbreviations

AR Aspect ratio
HR Hub/tip ratio
LE Leading edge
Opt Optimal
Ori Original
PS Pressure side
SS Suction side
TE Trailing edge

1 Introduction

At present, high load, high efficiency, wide operating range and dimension minimization are the goals of advanced high pressure compressor designs. In high pressure multistage axial compressors with small and medium dimensions, blades of rear stages are usually very short and thin. Thus, problems of insufficient compression work capacity, low efficiency and difficult machining may appear in axial compressor rear stages. In the condition that the axial compressor load has reached its limit, one of the common retrofit solutions is the axial-centrifugal compressor in which the rear axial stages are replaced with a centrifugal compressor. Both the load capacity of rear stages and the overall surge margin can be improved. However, a large flow path turning is usually inevitable to turn outlet radial channel into axial channel in order to connect the combustion chamber inlet in a centrifugal compressor designed for aero-engines. The radial dimension is increased, and the flow capacity is

Technical Editor: André Cavalieri.

✉ Jiang Chen
chenjiang27@buaa.edu.cn

✉ Jinxin Cheng
chengjinxin@iet.cn

Hang Xiang
xhyyyh@buaa.edu.cn

1 School of Energy and Power Engineering, Beihang University, Beijing, China

2 Institute of Engineering Thermophysics, Chinese Academy of Sciences, Beijing, China

3 Beijing Research Institute of Precise Mechatronics and Controls, Beijing, China

weakened. Hence, the axial-centrifugal compressor scheme may not meet the design requirements for a high pressure compressor with a limited radial dimension, an axial outlet channel and larger flow rate.

The mixed-flow compressor works with a higher mass flow and a higher efficiency than centrifugal compressors. Meanwhile, it has a higher load capacity: than axial compressors. This type of machine possesses advantages of both axial and centrifugal compressors. At present, one of hot researches for combined compressors in small and medium-sized aero-engines is designing high-performance mixed-flow compressors to replace axial or centrifugal compressor stages. Mixed-flow stages were adopted to replace front stages of multistage compressors in most compressor modification design processes according to previous researches. One of retrofit compressor configurations is the mixed-flow-co-centrifugal compressor that can replace axial-centrifugal or twin-stage centrifugal compressors in turboshaft engines[1–3]. The compressor axial dimension can be reduced, but the flow capacity is still weak on account of the complex flow path structure. The other configuration is the mixed-flow-co-axial compressor. The mixed-flow stage is connected to the axial-flow stage forepart [4, 5]. This kind of configuration has higher flow capacity and simpler flow path structure. However, larger hub radial dimensions of rear axial stages are adverse to the structure weight reduction.

The axial-co-mixed-flow compressor is an unconventional compressor configuration, in which a mixed-flow compressor stage is adopted to replace the axial compressor rear stages. The load capacity can be improved, and the axial dimension can be reduced compared with that of the multistage axial compressors. On the other hand, the axial-co-mixed-flow compressor possesses higher flow capacity, smaller radial dimension and smoother flow path than axial-centrifugal compressors. In order to minimize the axial length, the flow path transition section between the front axial stages and the final mixed-flow stage in this kind of compressor is extremely short or even negligible. Thus, the corresponding mixed-flow impeller usually has a high inlet hub/tip ratio and a low aspect ratio.

Some researchers have investigated the structure particularities of high hub/tip ratio centrifugal compressors. Groh et al. [6] presented the design and test results of an unusual high hub/tip ratio centrifugal compressor with a pressure ratio of 2.0. It was designed as a substitute of the last stages of a multistage axial compressor. Rodgers and Brown [7] summarized and compared various existing high hub/tip ratio centrifugal compressor designs. Sun [8] illustrated special considerations for the aerodynamic designs of high inlet hub ratio centrifugal compressors. Long and Wang [9] analyzed and improved a high hub/tip ratio centrifugal compressor as a retrofit design for a common centrifugal compressor. In general, adopting a high hub/tip ratio centrifugal compressor design to an axial-centrifugal compressor is conducive to the structure compaction and the performance improvement of the axial compressor stage. However, relative Mach number at the centrifugal compressor stage inlet rises with increasing hub/tip ratio, which may increase the impeller diffusion load and affect the centrifugal stage efficiency. [11] Hence, the high hub/tip ratio impeller configuration is a kind of compromise design in comprehensive consideration of overall dimensions and performance of each stage. It is applicable to the aerodynamic design schemes for the combined compressors with specific performance indexes and dimensional limit. Further, the high hub/tip ratio mixed-flow compressor configurations are more unconventional and there are few relevant researches on detailed designs and analyses for now. The only similar research on this compressor type is a mixed-flow compressor with a high inlet hub/tip ratio of 0.686 and a low aspect ratio proposed by Musgrave and Plehn [10] in 1987. Two types of mixed-flow compressors, respectively, investigated by Huang et al. [11], and Liu and Yu [12] were also adopted to connect the axial compressor stages outlet. However, the hub/tip ratios of the two compressors are relatively low so that the structure particularities are not obvious. In consideration of the special geometric features of high hub/tip ratio mixed-flow impellers, usual radial impeller design experience such as the performance prediction models and the selection methods of blade number and splitter blade length may be unsuitable. Hence, design criterions and aerodynamic optimizations are necessary to be improved and performed to achieve higher performances.

In this research, targeting the load capacity improvement and the axial dimension reduction, the aerodynamic retrofit design schemes for a four-stage high-load axial compressor are compared and screened. The high hub/tip ratio mixed-flow compressor is the decisive part in the retrofit design process. The optimal blade number and splitter blade length of the mixed-flow impeller are selected based on an improved loss model. A full-surface parameterization control method and the multi-island genetic algorithm are applied to blade optimizations for the mixed-flow compressor. The performance of the axial-co-mixed-flow compressor (as the principal retrofit design) is numerically simulated and analyzed. In addition, in order to further reduce the axial dimension and improve the load capacity, the preliminary designs of a twin-stage mixed-flow compressor and a twin-stage counter-rotating mixed-flow compressor, respectively, equipped with the high hub/tip ratio mixed-flow compressor are also proposed and explored.

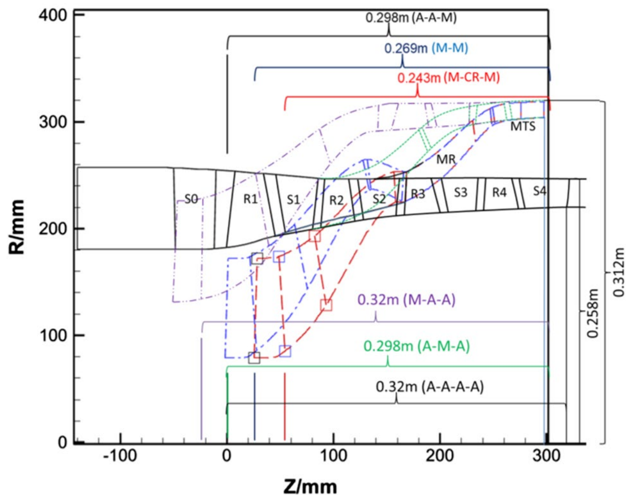

Fig. 1 Comparisons among various retrofit design schemes and the original design

Table 1 Design index parameters

Parameters	Unit	Value
Inlet total temperature	K	288.15
Inlet total pressure	Pa	101325
Mass flow rate	kg/s	18
Total pressure ratio	–	6.3
Rotate speed	rpm	14500
Outlet absolute Mach number	–	≤0.3
Overall axial length	m	≤0.3
Radial dimension	–	Least possible
Inlet and outlet flow direction	–	Axial

2 Discussion on retrofit design schemes

The original high pressure compressor is a four-stage axial compressor (A-A-A-A) with an average stage pressure ratio of 1.585, as shown in Fig. 1. According to the design index parameters presented in Table 1, the axial and radial dimensions are limited to reduce the structure weight. The direction and magnitude of the outlet velocity are also limited. Reducing stage number is the most effective way to meet the requirements for the axial dimension since the rotate speed is relatively low for high pressure compressors and there is a high demand for the stage load capacity. Five novel types of flow path retrofit configurations are conceived to reduce the stage number and raise the average stage load:

- •axial-co-mixed-flow compressor (A-A-M)
- •axial-co-mixed-flow-co-axial compressor (A-M-A)
- •mixed-flow-co-axial compressor (M-A-A)
- •twin-stage mixed-flow compressor (M-M)
- •twin-stage counter-rotating mixed-flow compressor (M-CR-M)

Figure 1 shows the flow path configurations and the axial dimensions of various design schemes. Stage loading levels of each scheme are evaluated based on Smith diagram and Cordier line, respectively, as shown in Figs. 2 and 3.

Figure 2 locates the efficiency zone positions of each stage in the axial compressor Smith diagram given by Hall [13]. Based on this load evaluation criterion, the third stage of A-A-M has very high Ψ and its location is beyond the efficiency border. It means the third stage has a weak flow capacity and a high load which a single axial compressor stage can hardly achieved. It is suitable to apply the mixed-flow compressor stage in the third stage to raise the load. Ψ and ϕ for Smith diagram are calculated by Equation (1).

$$\Psi = \Delta H / U_1^2 \quad \phi = 4Q_1 / \pi D_1^2 U_1 \tag{1}$$

However, Smith diagram is just appropriate for the axial turbomachinery. It can be only used as a reference for load evaluation of the mixed-flow compressor, while Balje line or Cordier line is normally adopted for the load evaluation and selection of the radial compressors. Figure 3 shows the load levels of the mixed-flow compressor stages of each retrofit configuration in a modified Cordier diagram given by Casey [14]. The locations of the axial compressor stages are also presented. Apparently, the modified Cordier diagram is applicable to the mixed-flow compressors rather than the axial

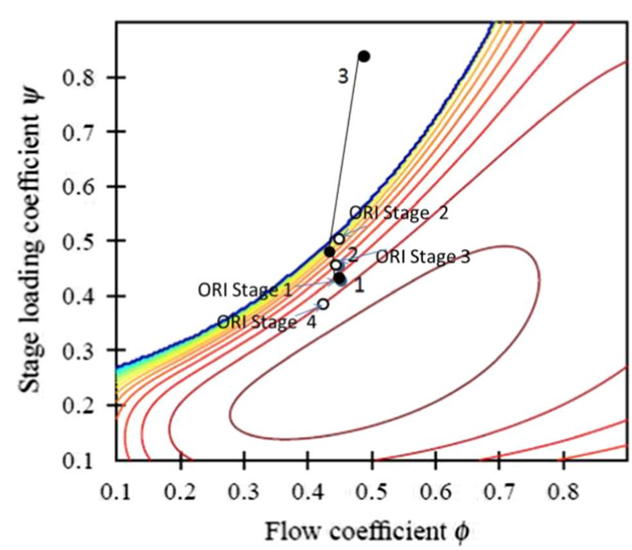

Fig. 2 Load locations of each stage of A-A-A-A and A-A-M in axial compressor Smith diagram; contour increment: 1%, peak contour: 95%

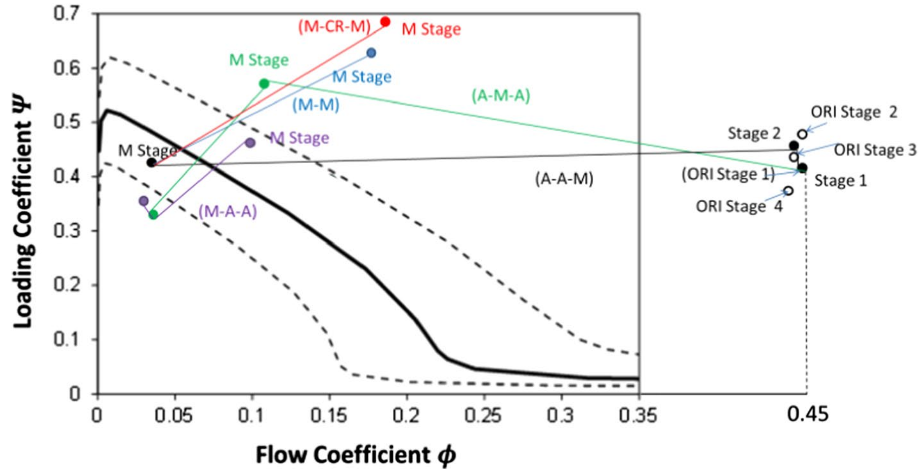

Fig. 3 Load locations of each stage of various retrofit design schemes and the original design in Cordier Diagram

Table 2 Main geometric parameter comparisons of the retrofit configurations and the original design

Type	A-A-A-A	A-A-M	M-M	M-CR-M
Axial length/m	0.320	0.298	0.269	0.243
Relative variation	–	−6.9%	−15.9%	−24.1%
Inlet tip radius/m	0.2590	0.2590	0.1719	0.1719
Relative variation	–	0	-33.6%	-33.6%
Outlet tip radius/m	0.258	0.312	0.312	0.312
Relative:variation	–	+20.9%	+20.9%	+20.9%
Inlet HR	0.676	0.676	0.460	0.460
Outlet HR	0.861	0.949	0.949	0.949
Stage number	4	3	2	2
Row number	9	8	5	4

compressors. The load levels of the axial compressor stages are out of the efficient boundary. Definitions of Ψ and ϕ for the Cordier line are different from that for Smith diagram, as described by Equation (2).

$$\Psi = \Delta H/U_1^2 \quad \phi = 4Q_1/\pi D_1^2 U_1 \tag{2}$$

Considering the inlet flow path connection and the outlet dimensions of the mixed-flow stage, the load position can hardly reach the best efficiency line in the condition of the design index. The location of the high hub/tip ratio mixed-flow compressor in A-A-M is the closest to the peak efficiency zone among the mixed-flow stages of all the schemes. Ψ of the mixed-flow compressor at the last stage locates at a relatively low level, which indicates the mixed-flow compressor possesses greater load-carrying potential. Hence, using mixed-flow compressors to decrease the stage number is an applicable solution for the retrofit designs of multistage axial compressors. As demonstrated in Fig. 1, M-A-A has a larger axial length and the rear two axial compressor stages with extremely high hub/tip ratios can hardly achieve the required efficiency and pressure ratio, while the middle mixed-flow stage of A-M-A has more serious interstage matching problems with the front and rear axial stages. Thus, this research only discusses A-A-M, M-M and M-CR-M. Main geometric parameters of the three modifications and the original compressor are compared in Table 2. The axial length is defined as the distance from the leading edge at the hub of the first rotor to the trailing edge at the hub of the last stator. Although the rear radial dimension enlarges, reductions of the axial and inlet radial dimensions as well as the row number are significant.

Two types of twin-stage mixed-flow compressors (M-M and M-CR-M) are also proposed to further explore the application of the high hub/tip ratio mixed-flow compressor. Based on the same design index presented in Table 1, the axial dimension needs to be least possible. The twin-stage mixed-flow compressor with no return channel is a novel combined compressor type which has a smoother flow path and a lower axial length. The second stage is the high hub/tip ratio mixed-flow compressor studied in this research. Both inlet and outlet flow directions are axial.

The current study only presents two preliminary design results for twin-stage mixed-flow compressors, as contrasts to A-A-M. The geometries of A-A-M, M-M and M-CR-M are shown and compared in Table 2 and Fig. 4. Their performances at $1.0R_n$, $0.9R_n$ and $0.8R_n$ are simulated by CFD software NUMECA. As presented in Fig. 5, only A-A-M can work stably at low rotate speeds for now. Obviously, the surge margins of M-M and M-CR-M are lower than that of A-A-M. There is a performance gap between M-M and A-A-M, while M-CR-M has much poorer performance. The main cause of performance degradation is the interstage matching problem between the front and the rear stages in twin-stage mixed-flow compressors. Nonetheless, the structures with no return channel of the three novel combined compressors are all beneficial for the reduction in dimension and cost, which

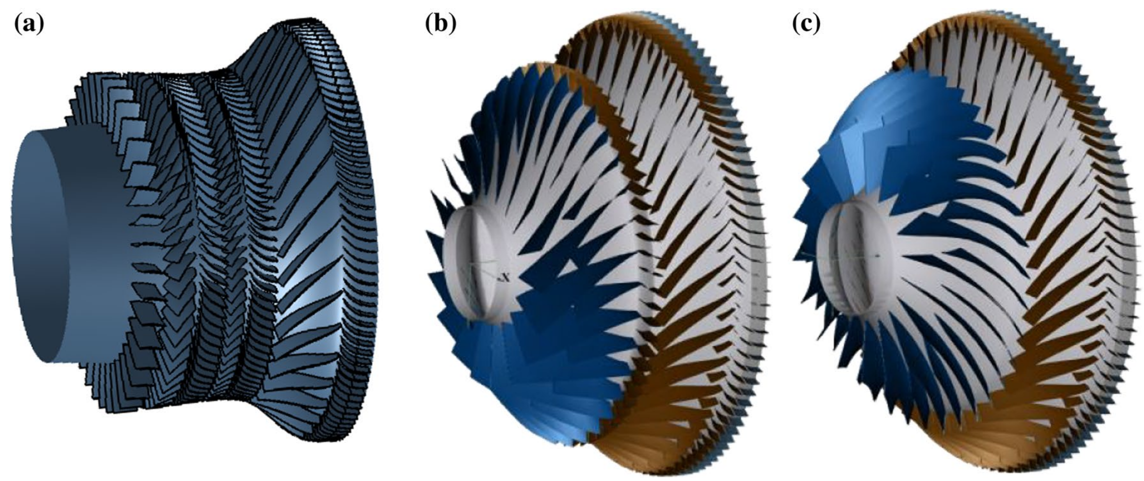

Fig. 4 3D geometries of the three kinds of combined compressor configurations with no return channel: **a** axial-co-mixed-flow compressor, **b** twin-stage mixed-flow compressor, **c** twin-stage counter-rotating mixed-flow compressor

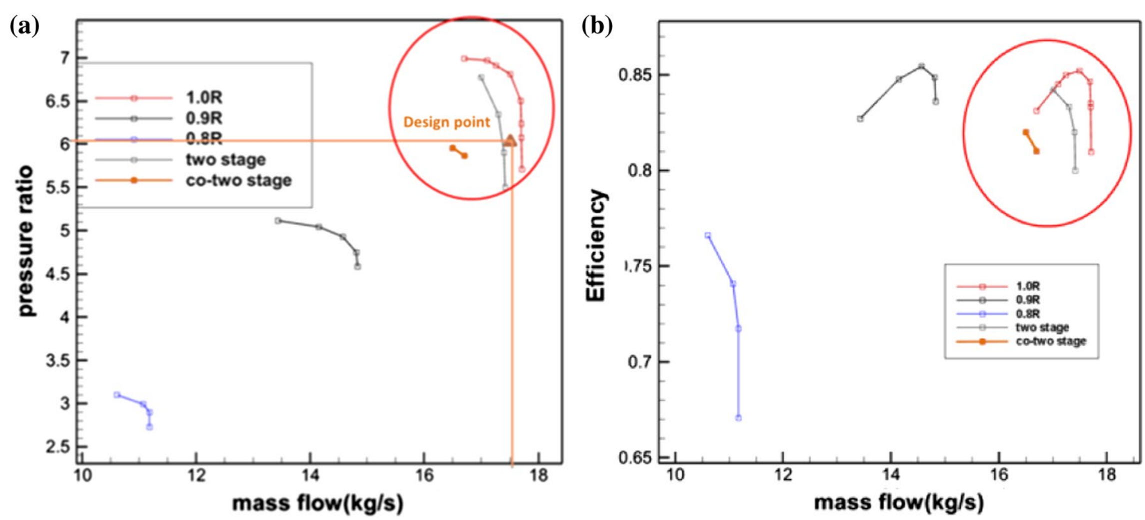

Fig. 5 CFD simulated performance comparisons of the three combined compressor configurations: **a** total pressure ratio, **b** adiabatic efficiency

shows the potential application prospects of high hub/tip ratio mixed-flow compressors.

For A-A-M, in order to take the furthest advantage of high flow capacity and high efficiency of the axial compressors, the axial compressor configuration is used in the front two stages which have better flow conditions. The IGV and the rotor of the first stage remain unchanged. The hub line rises from the stator inlet of the first stage, as demonstrated in Fig. 1. The loss caused by the mixed-flow configuration in the final stage can be offset. On the other hand, the mixed-flow stage strengthens the compression work capacity and has a wide stable operating scope to cope with a worse flow condition. Hence, A-A-M can improve the compressor load capacity with slight impact on the efficiency and the surge margin. Beyond that, A-A-M has a simpler flow path structure and moderate axial and radial sizes. It is beneficial to reduce the cost of structure dimension and manufacture. Above all, A-A-M is selected to be the principal retrofit scheme.

Increasing the outlet diameter can reduce Ψ, but ϕ declines more quickly. Conversely, decreasing the outlet diameter can increase ϕ and benefit the through flow. However, the centrifugal force does less work and Ψ raises. It is easier to cause the insufficient compression work and the flow separation. The mutual contradiction enhances the design difficulties of the high hub/tip ratio mixed-flow compressor. Advanced design methods and comprehensive

Table 3 The mixed-flow impeller design parameters (mean streamline)

Parameters	Unit	Value
T_1^*	K	410.15
P_1^*	Pa	320000
$\dot{m}$	kg/s	18
$\pi_r{}^*$	–	2.2
L_z	mm	79.8
δ	mm	0.3
r_2	mm	304
r_1	mm	239
b_2	mm	16
b_1	mm	51
γ_2	°	31.72
γ_1	°	24.75
β_2	°	38
$(d\beta/dm)_2$	°/m	−39.24

*means the total parameter

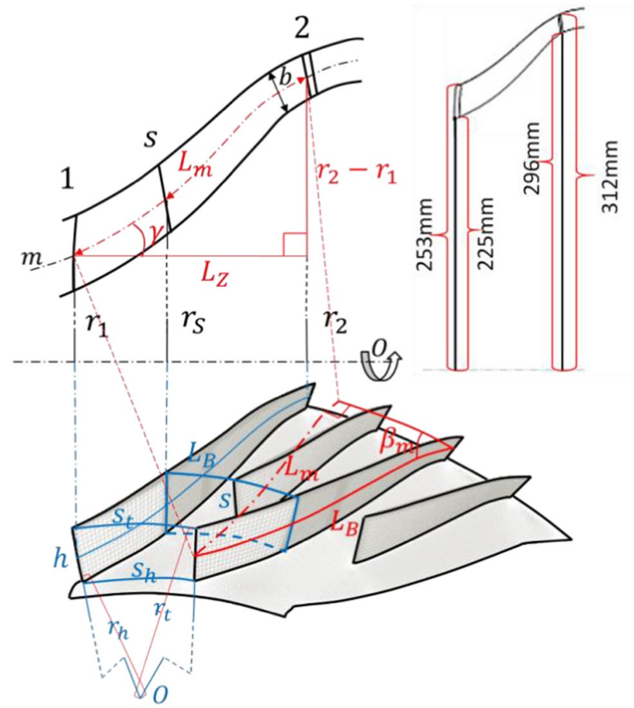

Fig. 6 Geometric parameters of the mixed-flow impeller

considerations of various factors are needed to achieve the performance requirements.

3 Improved design and optimization for the high hub/tip ratio Mixed-flow compressor

3.1 Analysis of Mixed-flow impeller dimensionless parameter

Table 3 presents the design parameters of the mixed-flow impeller without splitter blades. Detailed geometric descriptions are demonstrated in Fig. 6, including the meridional flow path, the blade chord length estimation and the definition of blade height/pitch ratio in cascades.

In this study, the dimensionless splitter blade length is defined as the length ratio of splitter blade and principal blade, as formulated by Equation (3).

$$\zeta = \mathrm{L_s}/\mathrm{L_B} \tag{3}$$

An improved loss model [15] that introduces blade number (Z) and dimensionless splitter blade length (ζ) is applied to select the optimal blade number and the optimal splitter blade length for the minimum head loss of the mixed-flow impeller. In the improved model, the splittered impeller is assumed to be divided into two tandem normal impellers: “1-S” and “S-2” to utilize existing normal impeller performance prediction models, as illuminated in Fig. 6. “S” means the splitter blade inlet. “S-1” is a no-splittered section with truncated principal blades, and “S-2” contains double splitter blades. The loss model modification for the splittered impellers refers to the performance prediction models proposed by Aungier [16] in consideration of incidence, skin friction, loading, clearance leakage and wake mixing. Krain impeller was adopted for model verification. The optimum blade number and splitter blade length are studied at the design flow rate. Detailed description of the improved loss model can be referred in Reference [15].

At present, the definition of the mixed-flow compressor impeller is broad and vague. Case (a) [17] and Case (b) [18] presented in Fig. 7 can be both seen as mixed-flow configurations (‘mixed-flow compressor’ was what they were called by the authors in their papers). However, the former is more similar to the axial compressor, while the latter is more similar to the centrifugal compressor. The blade profiles of these two cases also indicate that Case (a) was designed with axial compressor design methods, while Case (b) was designed with centrifugal compressor design methods. Hence, the magnitude of flow path lean angle and the difference of inlet and outlet diameters determine the design reference for the mixed-flow impellers.

There have been several previous mixed-flow compressor design researches [19, 20] that adopted the centrifugal compressor design methods and experience. These mixed-flow impellers were seen as the centrifugal impeller modifications. This research object can also be treated as a centrifugal impeller retrofit design, as shown in Fig. 7 (c). Centrifugal impeller design methods are more suitable for this research object since the difference of inlet and outlet diameters and

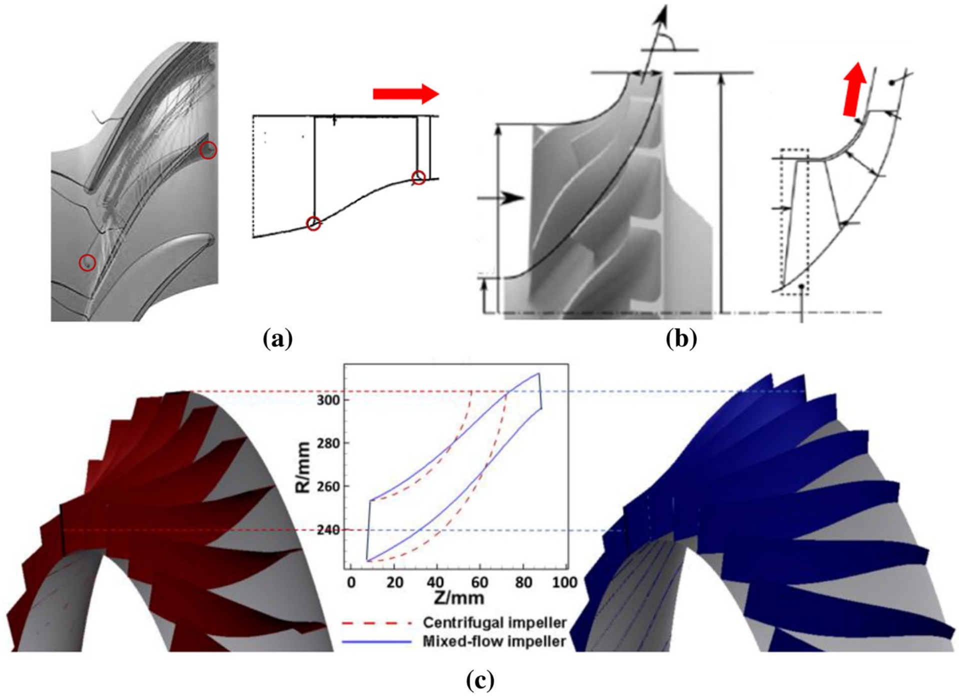

Fig. 7 Various mixed-flow impeller cases: **a** configuration similar to axial rotors [17], **b** configuration similar to centrifugal impellers [18], **c** this research object as a retrofit design for centrifugal impeller

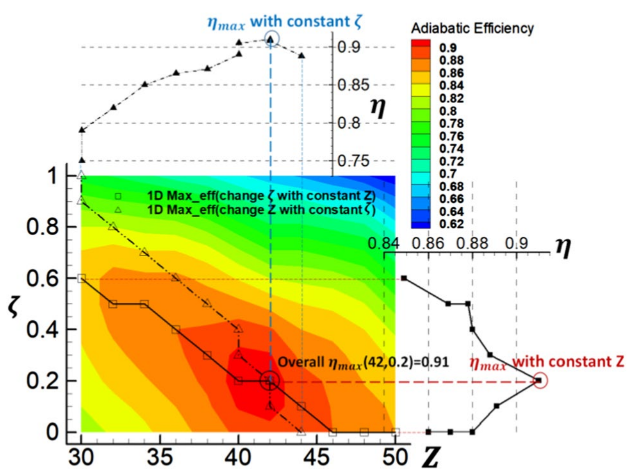

Fig. 8 Adiabatic efficiency distributions with respect to principal blade number and dimensionless splitter blade length

the flow path lean angle are relatively large. Meanwhile, high inlet hub/tip ratio and low aspect ratio cause the blade height of the mixed-flow compressor impeller to be comparatively low. Aerodynamic and geometric parameters vary moderately along the radial direction. Thus, the high hub/tip ratio mixed-flow impeller is peculiar and typical and it is more appropriate for the 1D mean streamline loss analysis. On the other hand, greater friction loss and clearance leakage loss may be caused by the increase in the relative blade surface area and the relative tip clearance, since the flow path is narrow and blade height is low.

Based on the improved 1D loss model, the distribution of impeller adiabatic efficiency at design flow rate with respect to Z and ζ is shown in Fig. 8. Variable ranges are Z = 30–50 and $\zeta = 0$ to 1.0 (particularly, $\zeta = 1.0$ means double principal blade numbers). High efficiency region locates where Z = 40–42 and $\zeta = 0$ to 0.2. The overall maximum efficiency is 0.91 and (Z, ζ) for the maximum efficiency is (42, 0.2). When Z and ζ are over-high or over-low, Efficiency declines rapidly. (Z, ζ) for overall minimum efficiency point is (50, 1). Two black lines that intersect in the $Z - \zeta$ plane represent the distributions of maximum efficiency points with respect to invariable and invariable ζ, respectively. Their intersection is the overall maximum efficiency point. ζ is approximatively linear with Z. On account of data range restriction, the vertical occurs at the left line end, but a linear extension can be predicted if data increase. The horizontal at the right line end demonstrates that splitter blades are unsuitable for the mixed-flow impeller design if blade number is overmuch.

Several previous models for selecting recommended blade number [15] are presented in Equation (4) as contrasts to the new model.

$$Z = \begin{cases} k_z \frac{d_1+d_2}{d_2-d_1} \sin & \text{(Galvas/Pfleiderer)} \\ \frac{2\pi \sin \beta_m}{0.4 \ln (d_2/d_1)} & (Ec\ker t) \\ 25 \sin \beta_2 / N_s & \text{(Rodgers)} \\ (90 - \beta_2)/2 & (Xu) \end{cases} \quad (4)$$

As illustrated in Fig. 6, the average blade chord length is estimated by:

$$Lc_m \approx \frac{r_2 - r_1}{\sin\gamma \sin\beta_m} \tag{5}$$

The average solidity is estimated by:

$$\tau_m \approx \frac{Lc_m}{s_m} \approx \frac{(r_2 - r_1)}{\sin\gamma \sin\beta_m} / \frac{2\pi(r_1 + r_2)}{2Z} \tag{6}$$

where s_m is average pitch.

The meridional streamline slope angle γ is 90° for radial impellers with no inducers. According to the cascade optimum solidity theory, the mixed-flow impeller can be regarded as an axially elongated radial impeller with no inducer. The optimum blade number is barely affected by γ. Hence, γ is set to 90° in the following discussion. $\tau_{m_{1-s}}$ and $\tau_{m_{s-2}}$ are obtained by applying Equation (6) to "1-S" and "S-2" parts of the mixed-flow impeller, as shown in Fig. 6. Equation (7) presents the formulas of τ_m, $\tau_{m_{1-s}}$ and $\tau_{m_{s-2}}$. Specifically, $\tau_m = \tau_{m_{1-s}}$ when $\zeta = 0$.

$$\begin{cases} \tau_m = \dfrac{Z}{\pi\left(\frac{r_1+r_2}{r_2-r_1}\right)\sin\beta_m} \\ \tau_{m_{1-s}} = \dfrac{Z(1-\zeta)}{\pi\left(\frac{r_1+r_2}{r_2-r_1}-\zeta\right)\sin\beta_m} \\ \tau_{m_{s-2}} = \dfrac{2Z\zeta}{\pi\left(\frac{2r_2}{r_2-r_1}-\zeta\right)\sin\beta_m} \end{cases} \tag{7}$$

Figure 9 shows the distributions of $\tau_{m_{1-s}}$ and $\tau_{m_{s-2}}$ with respect to Z and ζ. τ_m corresponding to the maximum adiabatic efficiency is approximately equal to 2 for no-splittered impeller configurations ($\zeta = 0$). The data contours also indicate that maximum efficiency points approximately locate at the region where $\tau_{m_{1-s}} + \tau_{m_{s-2}} = 2.25$. Thus, for the overall maximum efficiency point,

$$\begin{cases} Z = 2\pi\left(\frac{r_1+r_2}{r_2-r_1}\right)\sin\beta_m \\ \dfrac{Z(1-\zeta)}{\pi\left(\frac{r_1+r_2}{r_2-r_1}-\zeta\right)\sin\beta_m} + \dfrac{2Z\zeta}{\pi\left(\frac{2r_2}{r_2-r_1}-\zeta\right)\sin\beta_m} = 2.25 \end{cases} \tag{8}$$

Define $\overline{R} = (r_1 + r_2)/(r_2 - r_1)$ and ζ for maximum efficiency can be solved by Equation (9).

$$\frac{1-\zeta}{\overline{R}-\zeta} + \frac{2\zeta}{1+\overline{R}-\zeta} = \frac{1.125}{\overline{R}} \tag{9}$$

The new blade number empirical model in Equation (7) has the same form with Galvas' model [15] except that $k_z = 2\pi$. When the splitter blade is not considered, i.e., $\zeta = 0$, the new model will degenerate into Galvas' model. This model combines the cascade optimum solidity theory and the loss analysis. For the first time, the new model evaluates the splitter blade length quantitatively in detail and gives the analytical solutions of the blade number and the splitter blade length simultaneously. The adiabatic efficiencies of the no-splittered impeller configurations ($\zeta = 0$)

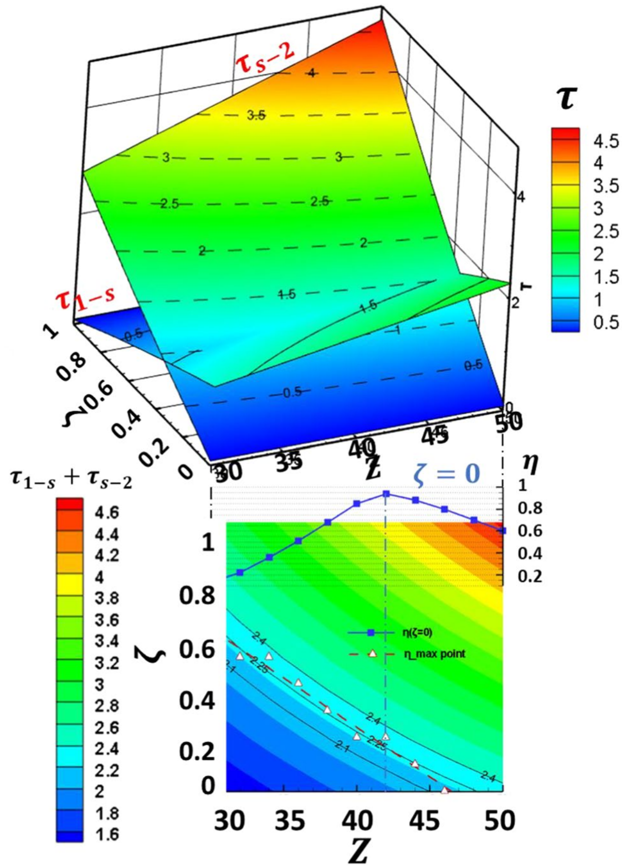

Fig. 9 Distributions of the average solidity and the maximum efficiency points

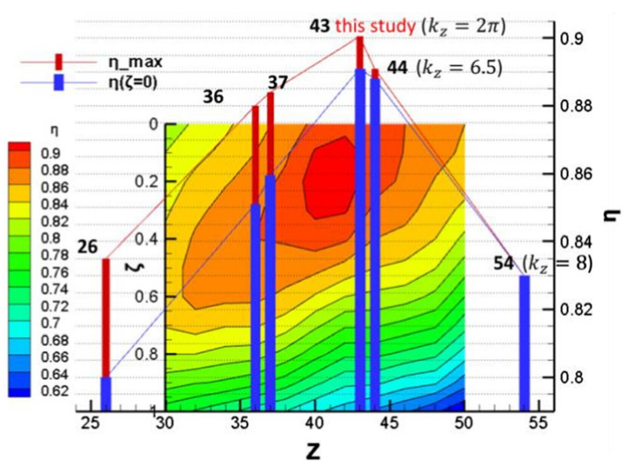

Fig. 10 Distributions of the average solidity and the maximum efficiency points

and corresponding maximum efficiencies for the optimum blade numbers calculated by the above models are shown in Fig. 10. It can be observed that blade number calculated by the new model is the closest to the high efficiency region among all the model results.

This study also investigates dimensionless cascade geometric parameters as a reference to select Z and ζ in consideration of the impeller geometric particularities of high hub/tip ratio and low aspect ratio. There are several typical dimensionless geometric parameters corresponding to different stream surfaces: hub/tip ratio ($\mathrm{HR} = \mathrm{r_h}/\mathrm{r_t}$, S2 surface), aspect ratio ($\mathrm{AR} = \mathrm{h}/\mathrm{L} = \left(\mathrm{r_t} - \mathrm{r_h}\right)/\mathrm{L}$, quasi-S2 surface) and solidity ($\tau = \mathrm{L}/\mathrm{s}$, S1 surface). However, the dimensionless geometric parameter corresponding to S3 surface has not been investigated in the previous studies. It can be defined as the blade height/pitch ratio ($\mathrm{h}/\mathrm{s_t}$). According to Fig. 6:

$$h/s_t = \left(r_t - r_h\right)/\left(2\pi r_t/Z\right) = (1 - HR)Z/2\pi = \tau \cdot AR \quad (10)$$

This parameter illustrates the relationship among blade number, hub/tip ratio, aspect ratio and solidity. Figure 11 presents distributions of $\mathrm{h}/\mathrm{s_t}$ and HR at ζ=0, 0.1, 0.2, 0.3, 0.4 and 0.5. Blade number needs to increase with higher HR for an invariable $\mathrm{h}/\mathrm{s_t}$. HR is higher, and $\mathrm{h}/\mathrm{s_t}$ is lower than the inlet values in the impeller rear channel, which means more blades are needed to maintain $\mathrm{h}/\mathrm{s_t}$ value and weaken the flow separation. Splitter blades are preferred in this case. There is an optimal $\mathrm{h}/\mathrm{s_t}$ to determine blade number and the leading edge position of splitter blade for each impeller configuration.

The off-design conditions and other additional losses such as supersonic loss have not been considered in the improved 1D loss model yet. The universality of the above models that describe the relation between Z and ζ still needs to be verified by more other impellers and experimental data.

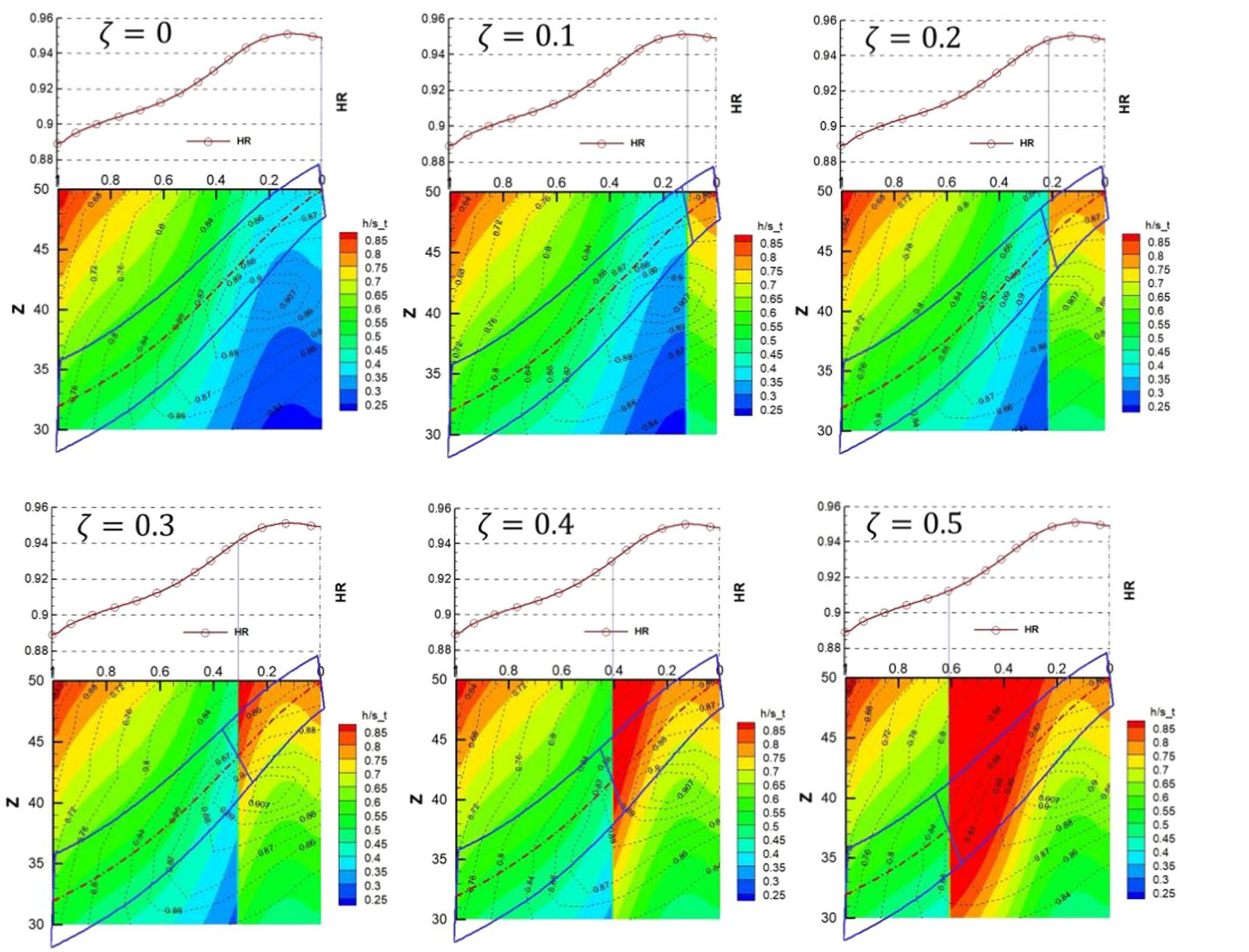

Fig. 11 Distributions of blade height/pitch ratio and hub/tip ratio

3.2 Aerodynamic optimization for the Mixed-flow compressor using Full-surface parameterization method

The three-dimensional aerodynamic optimization for compressors is a typical problem with the characteristics of high-dimension, elapsed time and black box (HEB). In order to solve this problem, the number of the optimization control parameters should be reduced on the premise that the optimal solution of the original design space remains unchanged. Hence, it is necessary to construct a parameterization technique with fewer control parameters and

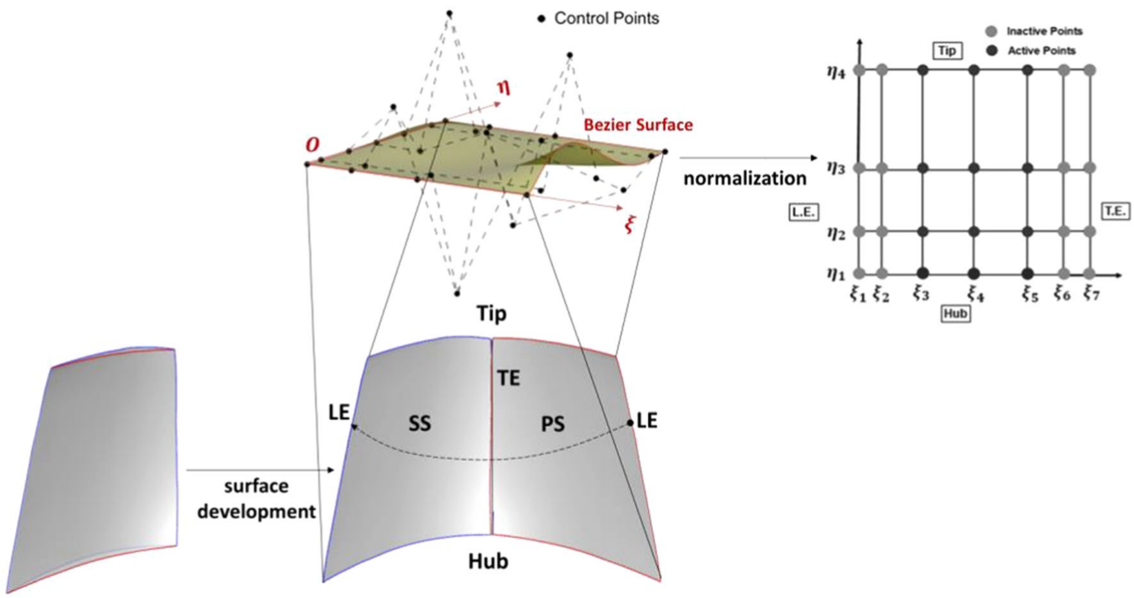

Fig. 12 Principle of the full-surface parameterization method

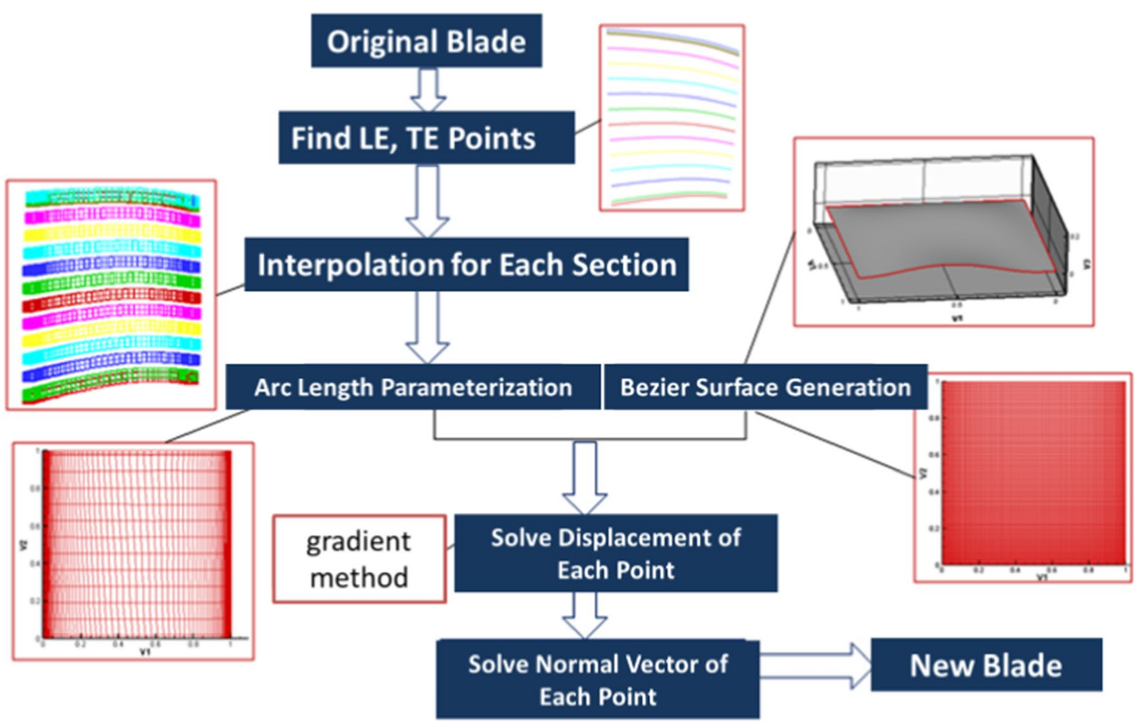

Fig. 13 Flowchart of parameterization

a better performance for compressor blade geometries. A full-surface parameterization control method is applied for blade optimization of the mixed-flow compressor. The principle and the flowchart of parameterization are presented in Figs. 12 and 13, respectively. In order to realize one-to-one mapping between physical domain points and calculation domain points, parametric arc lengths for the original surface points are calculated by:

$$\xi_{i,j} = \frac{\sum_{m=1}^{i} l_m}{L_j} \quad \eta_{i,j} = \frac{\sum_{n=1}^{j} ll_n}{LL_i} \tag{11}$$

where $\xi_{i,j}$ and $\eta_{i,j}$ are horizontal and vertical coordinates in the unit mesh plane, as shown in Fig. 12.

Displacement variations of calculation domain points for the original blade surface can be calculated by Bezier surface functions given by Equation (12).

$$\begin{cases} \vec{R} = \sum_{k=0}^{n} \left\{ \sum_{l=0}^{m} P_{k,l} B_l^m(v) \right\} B_k^n(u) \\ B_k^n(u) = C_k^n u^k (1-u)^{n-k} \\ C_k^n = \begin{cases} \frac{n!}{(n-k)!k!} if 0 \le k \le n \\ 0 \quad ifnot \end{cases} \end{cases} \tag{12}$$

where $\vec{R}$ is the normal displacement of each point in the calculation domain. $P_{k,l}$ represents the control points of the Bezier surface and the number of control points is $(m+1) \times (n+1)$. $B_l^m(v)$ and $B_k^n(u)$ are the Bernstein basis functions. C_k^n is combination number.

Burguburu and le Pape [21] Cheng [22], respectively, adopted the Bezier surface to control deformations of suction surfaces and pressure surfaces of axial compressor blades. The innovation point of full-surface parameterization control method is that the pressure surface and suction surface can be seen as one whole surface. As illustrated in Fig. 12, the Bezier surface is covered over the whole blade surface form leading edge to trailing edge and back to the original points. The trailing edge is the middle position of the whole surface. Displacements of the Bezier surface points correspond to the displacements of the original blade surface points. The smoothness of leading and trailing edges can be maintained, and optimization control variables can be reduced.

The multi-island genetic algorithm (population size 10, algebra 10 and population number 10) is adopted in the aerodynamic optimization of the mixed-flow compressor. There are three blade rows in the mixed-flow compressor stage. Each blade has twelve control points. As shown in Fig. 13, the red points are variable active control points and they can be moved along the surface normal direction. The green points are fixed control points, and they remain stationary to ensure the smoothness of the leading and trailing edge. The scopes of all variable are set to [-6, 6]. The optimization targets are the efficiencies of the near design point and the near stall point, respectively. The relative variation in flow rate is ±5%, and the pressure ratio is not less than the initial value. The optimization target function is given by:

$$\max f = \omega_{nd} * f_{nd} + \omega_{ns} * f_{ns} \tag{13}$$

The constraint conditions are given by:

$$\begin{cases} f_{nd} = eff_{nd}; \quad if \begin{cases} \left| \frac{m_{nd} - m_{nd_{ori}}}{m_{nd_{ori}}} \right| \le 5\% \\ P_{nd}^* - P_{nd_{ori}} \ge 0 \end{cases} \\ f_{ns} = eff_{ns}; \quad if \begin{cases} \left| \frac{m_{ns} - m_{ns_{ori}}}{m_{ns_{ori}}} \right| \le 5\% \\ P_{ns}^* - P_{ns_{ori}}^* \ge 0 \end{cases} \\ \text{else} \quad f_{nd} = \min us \, f_{ns} = \min us \end{cases} \tag{14}$$

At present, CFD approach represented by the numerical solution for RANS equation has been widely applied in the field of compressor aerodynamic designs. The influence of the random pulsation term in a unsteady flow is replaced by Reynolds stress, and turbulence models are introduced to enclose the equation. The computation load is greatly reduced compared with LES and DNS. However, boundary layer transition, turbulence model, losses of tip clearance, endwall, blade leading and trailing edge flow, and unsteady flow, etc., may increase the calculation error and uncertainty. The simulation should be verified with the test data as much as possible to maintain credibility and accuracy.

NUMECA software is adopted for 3D viscous steady turbulence simulations. The Spalart–Allmaras turbulence model is selected to simulate the compressor internal flow field. The space is discretized by the central difference scheme. Fourth-order Runge–Kutta method is used to solve the time derivative terms. The grids of single blade channel are generated by AutoGrid5 module of NUMECA. The mesh configurations of both the impeller and the tandem stator have H&I topologies. In order to ensure that the value of near-wall Y plus is less than 5, the first-layer grid spacing near the wall is set to 0.001 mm. Three kinds of grid densities are adopted to check mesh independence. The mesh configurations and grid numbers of no-splittered and splittered impeller configurations are presented in Table 4. The conditions of total temperature and pressure are imposed at the inlet boundary. Meanwhile, a condition of averaged static pressure is imposed at the outlet boundary. The inlet boundary conditions of the mixed-flow compressor and the A-A-M can refer to Tables 3 and 1 severally. The values

Table 4 Mesh configurations and grid numbers of different impeller configurations

	Mesh configuration	Grid number
No splitter blade	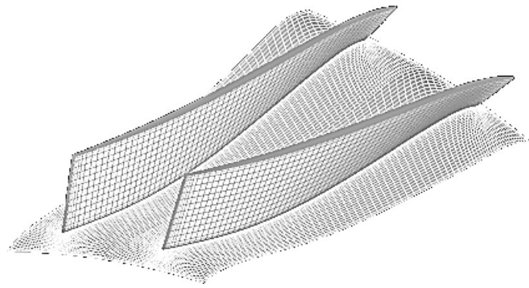	Mesh_1 499936 Mesh_2 894160 Mesh_3 1116184
Long splitter blade	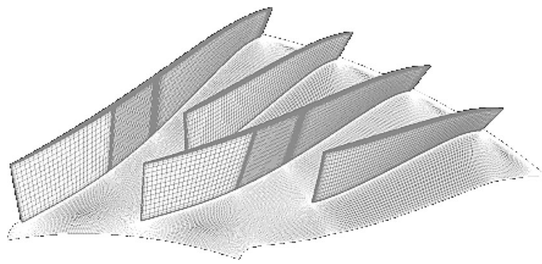	
Short splitter blade	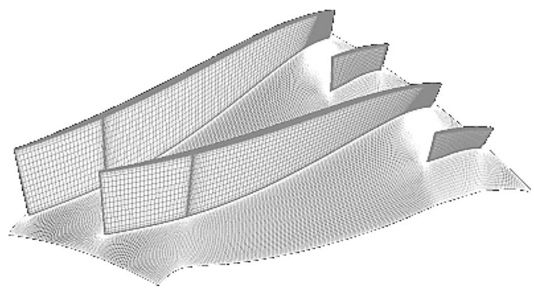	Mesh_1 667510 Mesh_2 1246180 Mesh_3 1813690

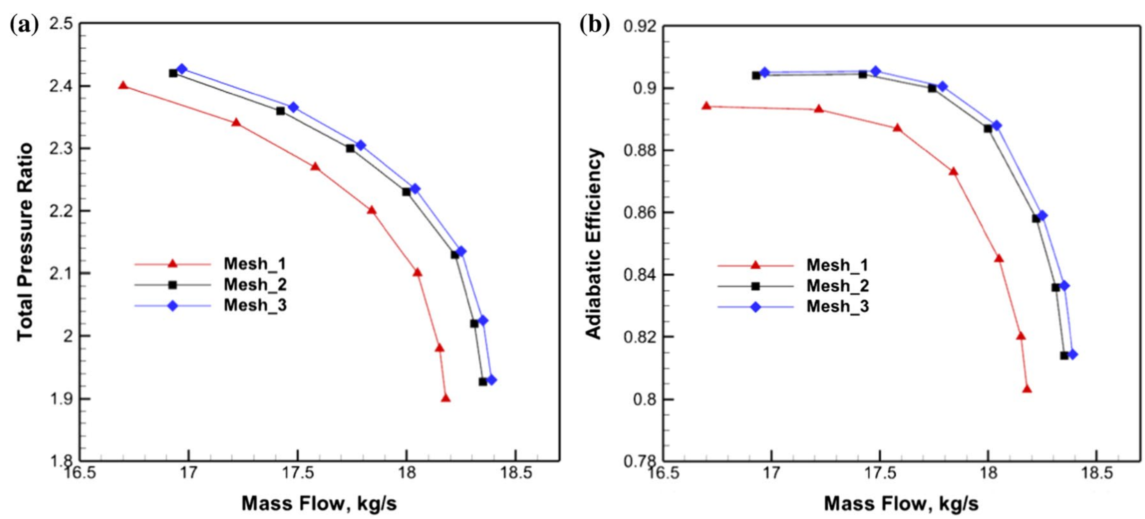

Fig. 14 Mesh independence verification: **a** characteristics comparison of total pressure ratio, **b** characteristics comparison of adiabatic efficiency

of outlet pressure are set to 600000Pa and 650000Pa corresponding to the near design point and the near stall point, respectively. The initial flow solution requires estimating the static pressure at the inlet, outlet and each rotor-stator interface. Considering the strong adverse pressure gradient flow in the compressor, the initial static pressure in front and rear of each blade usually needs to be estimated according to the blade load or calculated by the radial equilibrium control equation of the meridional flow surface. In the process of calculating a whole constant speed characteristic line, various operating points are calculated by changing the outlet back pressure. The calculation result of the adjacent previous operating point can be used as the initial condition for the current calculation. Figure 14 shows the performance comparisons of the original impeller simulated with different mesh configurations. The performance characteristics of Mesh_2 configuration and Mesh_3 configuration approach. Hence, Mesh_2 configuration is used for CFD numerical simulations in consideration of calculation accuracy and speed.

A cloud supercomputing service was used for the parallel calculation of this aerodynamic optimization. A thousand sample points with different blade geometries of the mixed-flow compressor were calculated on the supercomputing platform. Each calculation was executed with 6 CPU threads in about 15 minutes. The optimization process had taken about 31 hours in total using a 32-core x64-thread processor -- AMD Epyc™ 7452.

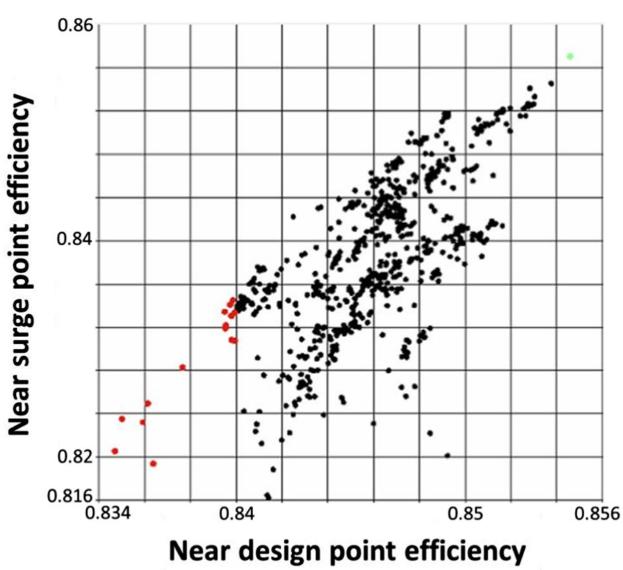

Fig. 15 Distribution of the sample points in the multi-objective optimization process

Figure 15 presents the distribution of sample points in this multi-objective optimization process. The green point represents the optimal mixed-flow compressor configuration which achieves the maximum adiabatic efficiency at both the near design point and the near stall point. The geometry comparisons of the optimal result and the original compressor are shown in Fig. 16. It can be seen that major geometric changes occur at leading edges of each blade row. Geometric variations are obvious at impeller tip and hub, the former stator hub and the rear stator tip. As indicated in Fig. 17, after optimization, the total pressure ratio increases by 3.71% relatively and the adiabatic efficiency increases by 0.95% absolutely at the near design point, while at the near stall point, the total pressure ratio and the adiabatic efficiency, respectively, increase by 5.55% relatively and 2.93% absolutely. There is a significant improvement on the performance of the mixed-flow compressor, especially at the near stall point.

The operation condition with a back pressure of 620000 Pa which is near the design point is selected to a benchmark to compare the flow field before and after the optimization. As shown in Fig. 18, the main flow loss occurs in the tandem cascade channel. The low kinetic energy flow exists in the front cascade of the tandem stator at the blade tip. Meanwhile, in the rear cascade channel, the mismatching of the inlet flow angle and the curve blade profile cause apparent separations at the leading edge of the pressure side and the trailing edge of the suction side. According to the static pressure distribution on the blade surface, it is observed that the optimization has improved the flow angle matching between the front and rear blade of the tandem stator. The large positive attack angle at the rear blade inlet has been eliminated. After the optimization, the region where the low kinetic energy flow and the separation flow occur are significantly reduced, especially at the blade tip and the midsection main flow region.

4 Performance of the Axial-co-mixed-flow compressor

The performances of the axial-co-mixed-flow compressor (A-A-M) at 1.0 R_n, 0.9 R_n and 0.8 R_n are calculated by 3D numerical simulation. In addition, the performances of the single mixed-flow compressor stage and the single mixed-flow impeller are also simulated.

The blade tip gap is 0.3 mm, and 17 mesh control volumes were put into the tip gap region. The distance from the first-layer grid to the wall is also set to 0.001 m to meet the requirement of the value of Y plus. The meshes and the values of near-wall Y+ of the three stages in A-A-M are

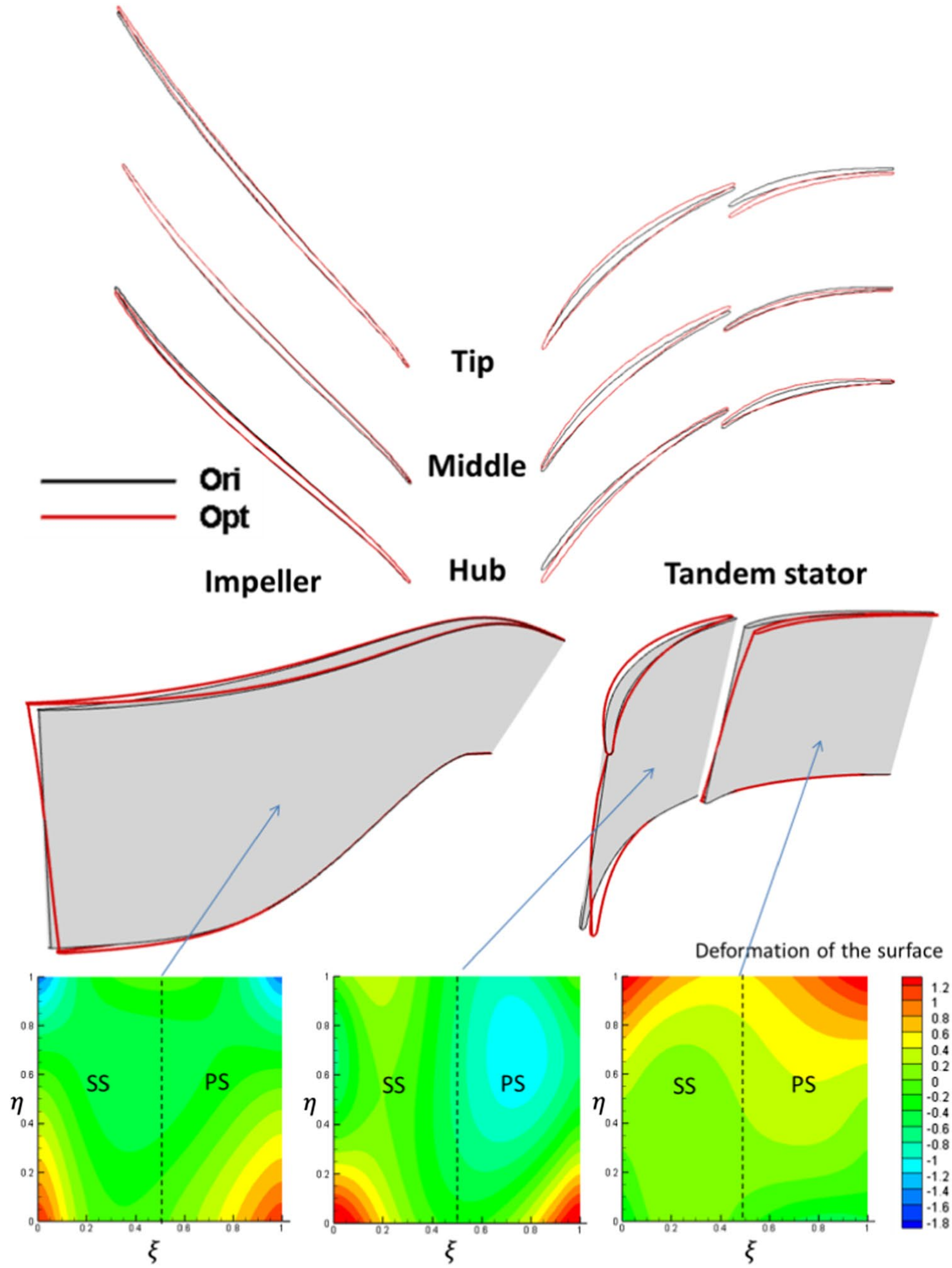

Fig. 16 Geometry comparisons of the optimized and original mixed-flow compressor

presented in Fig. 19. The total grid number of three stages of A-A-M is 2288014. The minimum skewness angle is 22.179°. The maximum aspect ratio is 5835.2. The maximum expansion ratio is 3.183. The values of Y+ near the wall are all lower than 5, which is appropriate for the S-A turbulence model.

Figure 20 presents the performances of the impeller, the mixed-flow compressor stage and A-A-M at three rotate speeds. The performance of the original four-stage axial compressor (A-A-A-A) is also presented as a comparison. As the rotate speed decreases, the total pressure ratio of A-A-M declines uniformly while the pressure ratios of the mixed-flow stage and the impeller decline more slowly. This indicates that the mixed-flow stage has a wider stable operation range and still carries a relatively higher load at the off-design conditions. Hence, the mixed-flow stage maintains a relatively higher load capacity than the front axial-flow stages. The peak pressure ratio of A-A-M is higher than that of A-A-A-A at 1.0 R_n and 0.9 R_n. At 0.8 R_n, the peak pressure ratio of A-A-M approaches that of

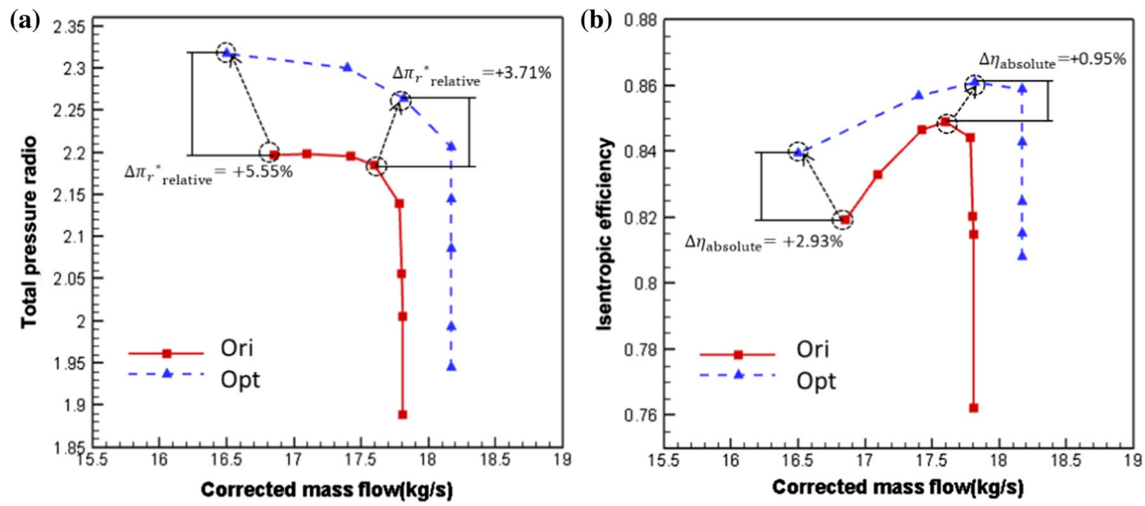

Fig. 17 Performances comparisons of the optimized and the original mixed-flow compressor: **a** total pressure ratio, **b** adiabatic efficiency

A-A-A-A with a slight decline. On the other hand, the flow rate declines after modification, especially at 0.8 R_n. In general, A-A-M has a higher load capacity than A-A-A-A, while the flow capacity of A-A-M is lower than that of A-A-A-A.

The efficiency of A-A-M maintains a relatively high level at 0.9 R_n and 1.0 R_n. However, the efficiency declines significantly and the efficiency characteristic curve steepens at 0.8 $\dot{R}$, which indicates the stability margin declines. The efficiency characteristic curves of the mixed-flow stage and A-A-M approach. Therefore, the efficiency performance of A-A-M is mainly influenced by the mixed-flow stage, while the efficiency of the impeller is still at a relatively high level at 0.8 R_n, which indicates that the tandem stator is the main factor that restricts the overall efficiency promotion. There is a slight efficiency difference between A-A-M and A-A-A-A. Although the peak efficiency of A-A-M is slightly lower than that of A-A-A-A, the load capacity improvement is much more obvious. Thus, the axial-co-mixed-flow compressor combination scheme may have some reference significance for dimension reductions and performance improvements of high pressure axial compressors.

At the near design point, the near choke point and the near stall point, the comparisons of blade angle and airflow angle at each blade row inlet in the mixed-flow compressor stage are shown in Fig. 21. Figure 21a shows that the flow angles at the hub and the middle of the impeller match relatively well. The negative attack angle exists near the tip region. The attack angle declines gradually as the stage load increases. The negative attack angle near the tip region is weakened. The positive attack angle appears at the hub and the middle of the impeller. As demonstrated in Fig. 21b, the positive attack angle exists from the hub to the tip of the former stator and rises gradually with the stage load increasing, which may cause flow separation at the suction surface. The maximum positive attack angle locates near the tip region. Fig. 21c shows that the flow angle at the rear stator inlet changes slightly along the radial direction due to low blade height. The negative attack angle exists from the hub to the tip. As the stage load increases, the attack angle variation is not apparent.

Figure 22 demonstrates that there is no obvious flow separation in the impeller cascade channel at the near design point. Main separation occurs in the hub region of the suction surface tail of the rear stator. A strong flow acceleration caused by the large positive attack angle occurs at the suction surface leading edge of the former stator, which corresponds to the positive attack angle region shown in Fig. 21b.

The geometric and the flow matchings with the former axial stages is the principal difficulty for the application of the mixed-flow compressor. The drastic curvature change of the mixed-flow impeller flow path is an important factor that causes flow losses. The impeller inlet and outlet relative positions and the axial-oblique turning angles of the flow path have direct effects on the flow path curvature. Therefore, interstage and rotor-stator flow path matchings are of vital importance. The impeller inlet axial transition is beneficial for the flow conditions at the axial-flow stage outlet and the mixed-flow stage inlet. However, a

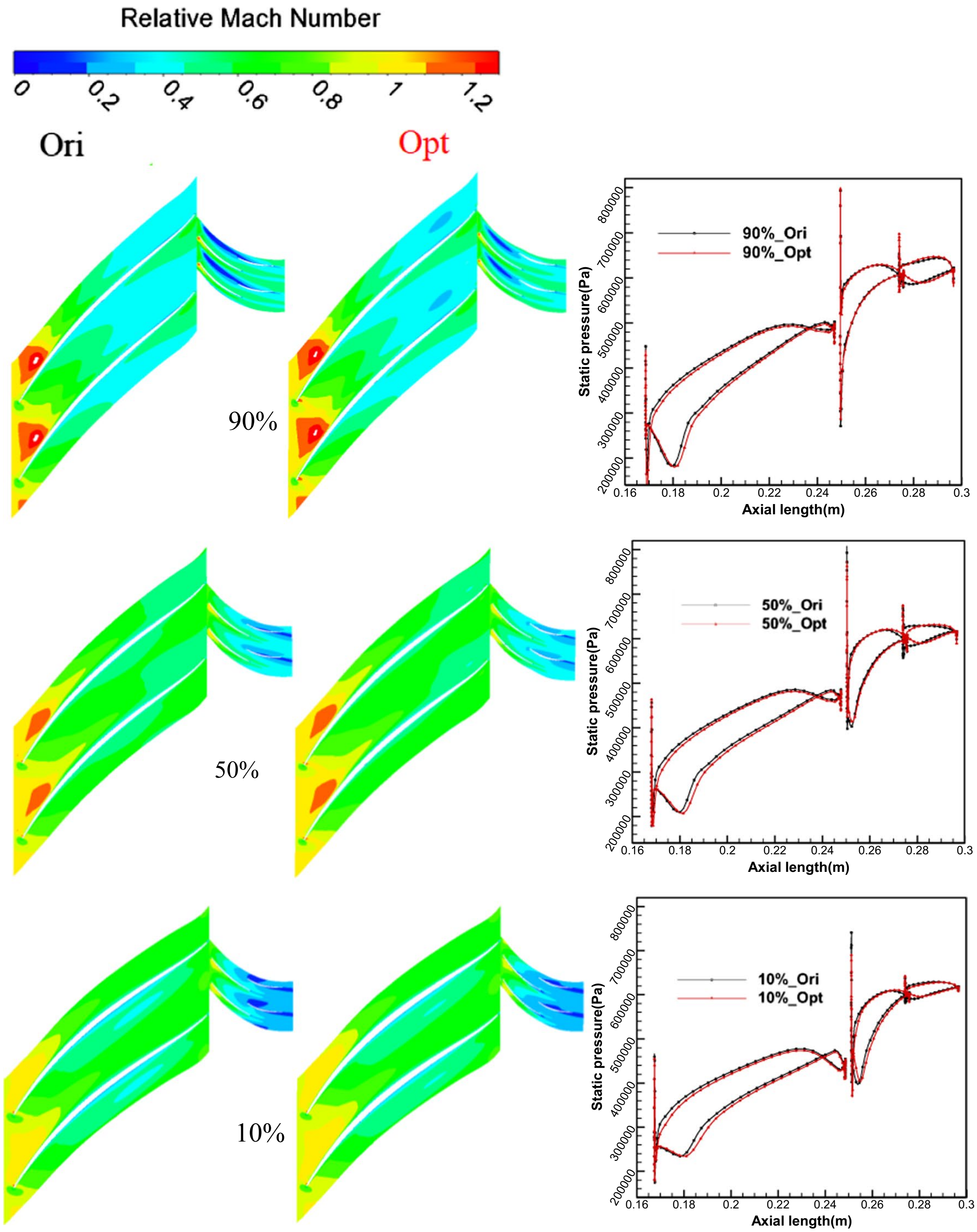

Fig. 18 Comparisons of the relative Mach number of S1 surface and static pressure on the blade surface

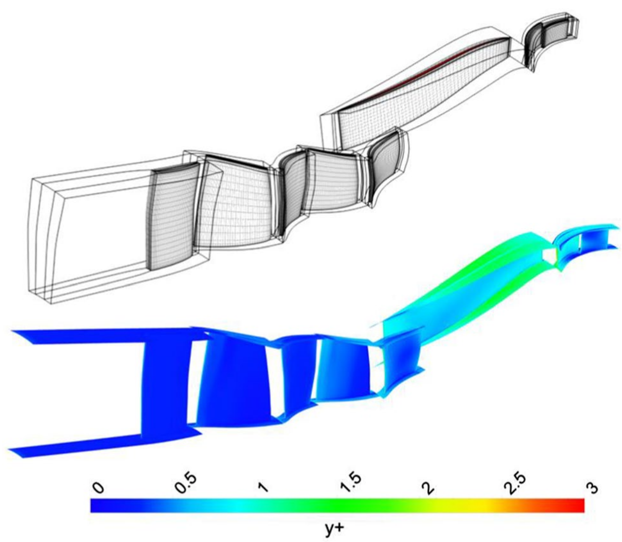

Fig. 19 The meshes and the near-wall Y+ of A-A-M

greater curvature change of the flow path is generated at the impeller inlet. Similarly, the impeller outlet axial transition may causes a large flow path turning and a curvature variation.

5 Conclusion

A high hub/tip ratio mixed-flow compressor and three novel retrofit design schemes for a high pressure axial compressor are proposed and investigated. The performance of the mixed-flow compressor and the axial-co-mixed-flow compressor has been improved using a full-surface parametric optimization approach. The conclusions are as follows.

(1) The high hub/tip ratio mixed-flow compressor can greatly promote the load capacity with slight impact on efficiency and surge margin. Meanwhile, simpler structures are beneficial for the reduction in axial dimension. The structures with no return channel of various high pressure compressor retrofit schemes demonstrate the potential application prospects of high hub/tip ratio mixed-flow compressors.
(2) The mixed-flow impeller configuration equipped with 42 principal blades and splitter blades with a fifth of principal blade length achieves the maximum adiabatic efficiency at the design flow rate. Blade height/pitch ratio which illustrates the relation among blade number, hub/tip ratio, aspect ratio and solidity can also be adopted as a reference for the selections of blade number and splitter blade.

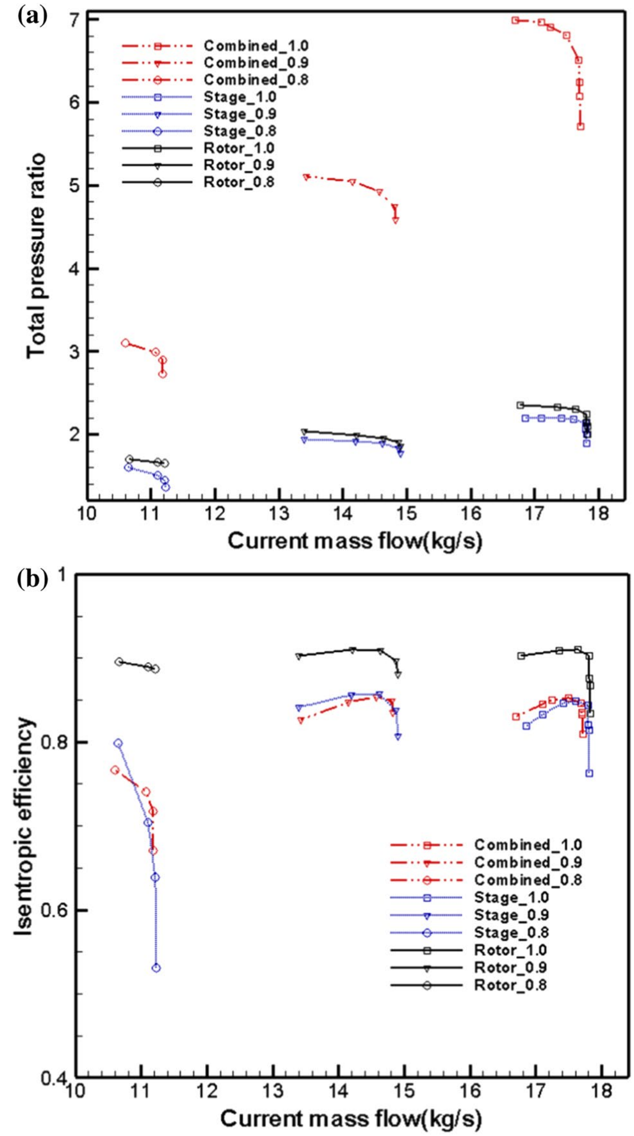

Fig. 20 Performances of impeller, mixed-flow stage and combined compressor: **a** characteristics of total pressure ratio, **b** characteristics of adiabatic efficiency

(3) Compared with the traditional optimization parametric methods, the full-surface parametric method can effectively decrease the control parameters and shrink the variation space of the variables in the optimization process. At the near design point, the total pressure ratio and the isentropic efficiency, respectively, increase by 3.71% relatively and 0.95% absolutely. At the near stall point, they, respectively, increase by 5.55% relatively and 2.93% absolutely, which shows a more significant performance enhancement. These improvements demonstrate the approach effectiveness in the reduction in the time as well as the dimensionality of the optimization control parameter space mapping. It is beneficial to

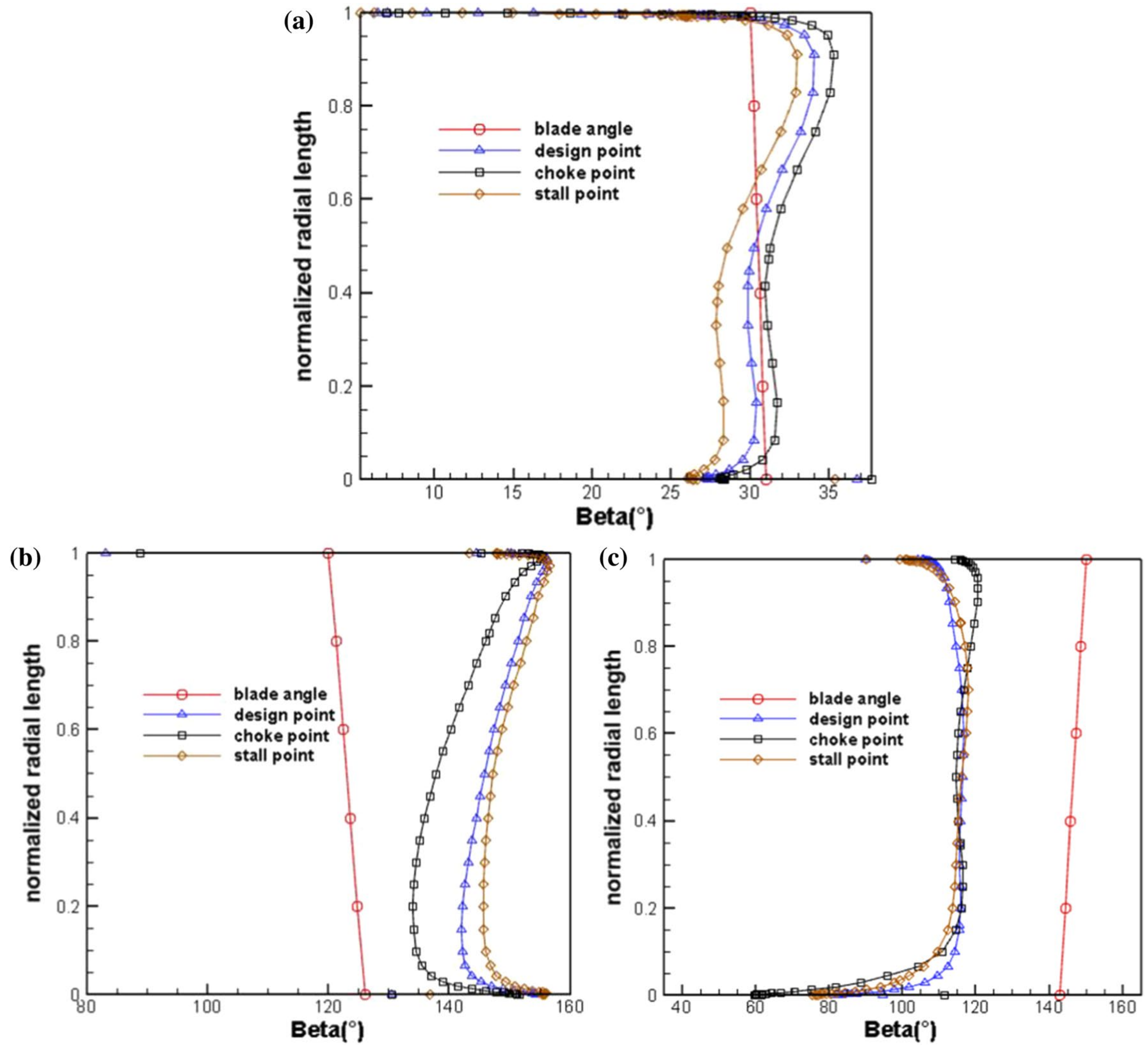

Fig. 21 Radial distributions of blade angle and airflow angle at each blade row inlet: **a** rotor, **b** front row of stator, **c** rear row of stator

solve the HEB frontier issue in the field of the compressor aerodynamic optimization.

(4) The axial-co-mixed-flow compressor is a considerable retrofit design scheme for high pressure axial compressors, which can meet the requirements of high load capacity and compact dimensions. It has some reference significance for dimension reductions and performance improvements of high pressure axial compressors. Further, the twin-stage (counter-rotating) mixed-flow compressor possesses even greater potential advantages in stage load capacity promotion and axial dimension reduction. The subsequence work is to further explore detailed aerodynamic designs and verify the feasibility of twin-stage mixed-flow compressors.

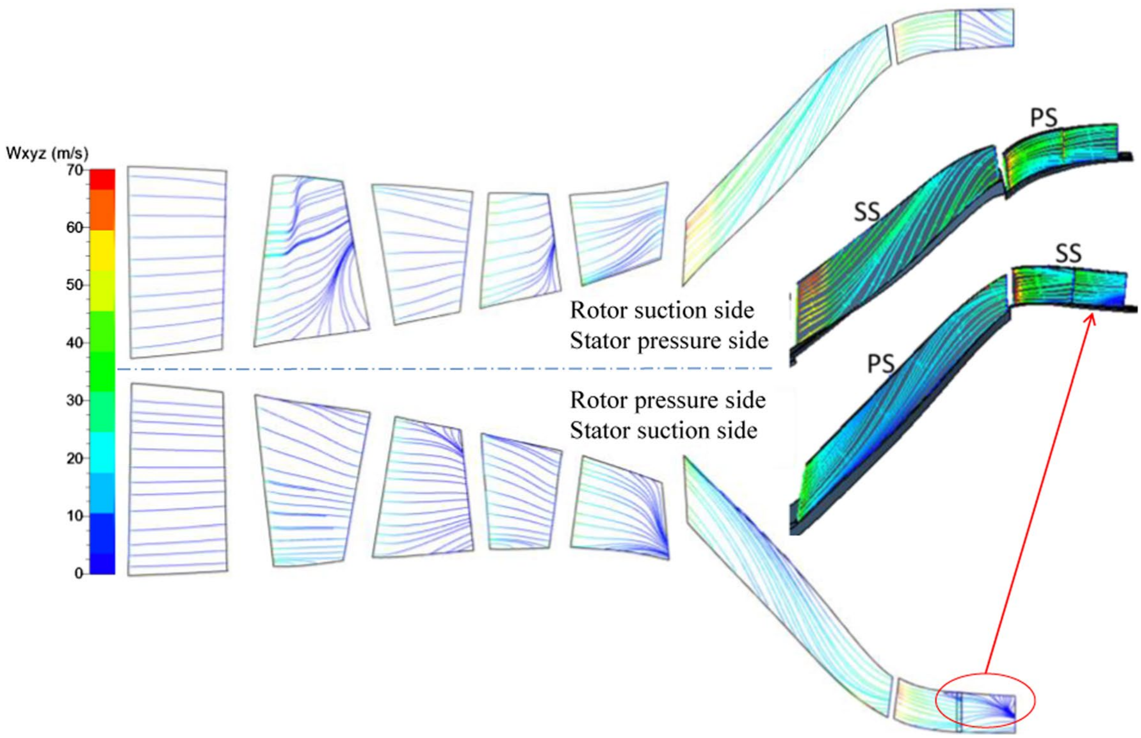

Fig. 22 Near-wall limit streamlines at the near design point

Appendix

Appendix: Springer-Author Discount

List of symbols

b	Append Hub-to-shroud passage width
D	Diameter
f	Optimized objective function
h	Blade height
L	Blade length
Lc	Blade chord length
$\dot{m}$	Mass flow
P^*	Total pressure
Q	Volume flow
R_n	Design rotate speed
R_n	Design rotate speed

$\overline{R}(\mathrm{r}_1 + \mathrm{r}_2)/(\mathrm{r}_2 - \mathrm{r}_1)$

r	Radius
s	Pitch
T^*	Total temperature
U	Blade tangential velocity
U	Blade tangential velocity
Z	Main blade number
β	Blade angle with respect to tangent
γ	Meridional streamline slope angle
ΔH	Total enthalpy increase
δ	Tip clearance
ζ	Dimensionless splitter blade length
η	Adiabatic efficiency, vertical coordinate
η	Adiabatic efficiency, vertical coordinate
ξ	Horizontal coordinate
π_r^*	Total pressure ratio
τ	Solidity
Ψ	Loading coefficient
ϕ	Flow coefficient
ω	Weight coefficient

Subscripts

B	Principal blade parameter
h	Hub
m	Meridional, mean
nd	Near design point
ns	Near stall point
ori	Original parameters (before optimization)
out	Outlet
s	Splitter blade (inlet)
t	Tip
z	Axial

1 Inlet
2 Outlet

Acknowledgements This study is supported by National Science and Technology Major Project (2017-II-0006-0019) and Civil Aircraft Special Project Research of China (MJZ-2017-D-30).

References

1. Cai X, Huang S, Tang F (2012) The design of High-loading Mixed-flow compressor. Enterp Sci Technol Dev 12:17–20
2. Lu X, Zhu J, Zhao S (2015) The ultra-compact high pressure mixed flow ratio—a combination of centrifugal compressor structure. CHINA Patent, CN102678590 B. 2015-08-12
3. Youssef N, Weir G (2002) Mixed flow and centrifugal compressor for gas turbine engine. USA Patent, US6488469. 2002-12-03
4. Zhang XY, Chen XY, Li LC et al (2018) Aerodynamic design and numerical simulation of mixed-axial flow multi-stage compressor. Chin J Ship Res 13(4):104–110
5. Xuanyu C, Xiangwei M, Xingmin G et al (2015) The aerodynamic design and investigation of loading distribution of a mixed flow compressor. Procedia Eng 99:484–490
6. Groh FG, Wood GM, Kulp RS et al (1970) Evaluation of a high Hub/tip ratio centrifugal compressor. J Fluid Eng 92:419–428
7. Rodgers C, Brown D (2009) High Hub/Tip ratio centrifugal compressors. In: Proceedings of the ASME turbo expo 2009: power for land, sea, and air, vol 7. ASME, Turbomachinery, Parts A and B, Orlando, Florida, USA, pp 1151–1161. https://doi.org/10.1115/GT2009-59012
8. Sun X (1982) (1982) Design of high inlet Hub/tip ratio centrifugal compressor. Turbine Technol 2:42–50
9. Long S, Wang Y (2011) Redesign and analysis of a high Hub/tip ratio centrifugal compressor. Fluid Mach 39(11):58–61
10. Musgrave DS, Plehn NJ (1987) Mixed-flow compressor stage design and test results with a pressure ratio of 3: 1. J Turbomach 109:513–519
11. Jian H, Zhenxia L, Zhong R et al (2011) Exploring numerically overall performance and flow field of mixed flow compressor stage with splitter blades. J Northwestern Polytech Univ 2:26
12. Liu Q, Yu Y (2013) Numerical analysis of mixed compressor tip clearance. J Propul Technol 34(2):168–172
13. Hall DK, Greitzer EM, Tan CS (2012) Performance limits of axial compressor stages. In: Proceedings of the ASME turbo expo 2012: turbine technical conference and exposition, vol 8. ASME, Turbomachinery, Parts A, B, and C, Copenhagen, Denmark, pp 479–489. https://doi.org/10.1115/GT2012-69709
14. Casey M, Zwyssig C, Robinson C (2010) The cordier line for mixed flow compressors. In: Proceedings of the ASME turbo expo 2010: power for land, sea, and air, vol 7. ASME, Turbomachinery, Parts A, B, and C, Glasgow, UK, pp 1859–1869. https://doi.org/10.1115/GT2010-22549
15. Xiang H, Chen J, Cheng J (2018) Optimum blade number and splitter blade length of a Mixed-flow impeller based on mean streamline loss model. 2018 joint propulsion conference. Cincinnati, AIAA 2018-4827. https://doi.org/10.2514/6.2018-4827
16. Aungier RH (1995) Mean streamline aerodynamic performance analysis of centrifugal compressors. J Turbomach 117(3):360–366
17. Zhu M, Qiang X, Huang T et al (2013) Investigation of tip leakage flow and stage matching with casing treatment in a transonic mixed-flow compressor. Int J Turbo Jet Eng 30(3):283–292
18. Diener OH, van der Spuy SJ, von Backström TW et al (2016) Multi-disciplinary optimization of a mixed-flow compressor impeller. In: Proceedings of the ASME turbo expo 2016: turbomachinery technical conference and exposition, vol 8. ASME, Microturbines, Turbochargers and Small Turbomachines; Steam Turbines, Seoul, South Korea. https://doi.org/10.1115/GT2016-57008
19. Whitfield A, Roberts DV (1981) The effect of impeller tip design on the performance of a mixed flow turbocharger compressor. In: Proceedings of the ASME 1981 international gas turbine conference and products show, vol 1. ASME, Aircraft Engine; Marine; Turbomachinery; Microturbines and Small Turbomachinery, Houston, Texas, USA. https://doi.org/10.1115/81-GT-7
20. Wang SJ, Yuan MJ, Xi G et al (1992) Development and industrial application of the "All-over-controlled vortex distribution method" for designing radial and mixed flow impellers. In: Proceedings of the ASME 1992 international gas turbine and aeroengine congress and exposition, vol 1. ASME, Turbomachinery. Cologne, Germany. https://doi.org/10.1115/92-GT-262
21. Burguburu S, le Pape A (2003) Improved aerodynamic design of turbomachinery bladings by numerical optimization. Aerosp Sci Technol 7(4):277–287
22. Cheng J, Chen J, Xiang H (2019) A surface parametric control and global optimization method for axial flow compressor blades. Chin J Aeronaut 32(7):1618–1634